ROYAL SOCIETY OF CHEMISTRY

Journal of
Materials Chemistry A

Correlating the Electrocatalytic Stability of Platinum Monolayer Catalysts to Their Structural Evolution in the Oxygen Reduction Reaction

SCHOLARONE™
Manuscripts

Correlating the Electrocatalytic Stability of Platinum Monolayer Catalysts to Their Structural Evolution in the Oxygen Reduction Reaction

Guangyu Chen,[a,b] Kurian A. Kuttiyiel,[b] Meng Li,[b] Dong Su,[c] Lei Du,[a] Chunyu Du,[a] Yunzhi Gao,[a] Weidong Fei,[d] Geping Yin,*[a] Kotaro Sasaki,*[b] Radoslav R. Adzic*[b]

[a] MIIT Key Laboratory of Critical Materials Technology for New Energy Conversion and Storage, School of Chemistry and Chemical Engineering, Harbin Institute of Technology, Harbin 150001, China

[b] Chemistry Department, Brookhaven National Laboratory, Upton, NY 11973, USA

[c] Center for Functional Nanomaterials, Brookhaven National Laboratory, Upton, NY 11973, USA

[d] School of Materials Science and Engineering, Harbin Institute of Technology, Harbin 150001, China

*To whom correspondence should be addressed. Emails: yingeping@hit.edu.cn; ksasaki@bnl.gov; adzic@bnl.gov.

1

Abstract

Platinum monolayer (Pt_{ML}) core-shell electrocatalysts for oxygen reduction reaction (ORR) have attracted great attentions because of their exceptional activity and stability for promising practical applications in fuel cells. Here, we describe our in-depth investigation of the relationship between the ORR activity and structure of Pt_{ML}/Pd/C catalyst during the stability test. By virtue of the rotating disk electrode technique, an accelerated degradation test with the potential window of 0.65 to 1.05 V was applied to the Pt_{ML}/Pd/C to interrogate its long-term reliability in the ORR, the change of its electrochemical surface area, and its surface composition and component. The Pt_{ML}/Pd/C catalyst displayed a volcano-like mass/dollar activity profile in the stability test up to 100k cycles. An overall loss of the activity was recorded to be as low as 17% of the initial value. The ORR activity increased in the initial 20k cycles because the freshly-prepared Pt_{ML} did not entirely encompass the whole Pd core, but it was integrated to a full coverage with a more stable configuration during the potential cycling owing to its self-healing property. Then, the activity descended at a much slower rate than the standard Pt/C because the Pd-Pt core-shell structure due to its structural self-retaining property remained intact and impeded the electrochemical Ostwald ripening of the entire particles. Changes in morphology and configuration of Pt_{ML} were mapped by combining our experimental investigation with model analyses. The proposed self-healing and self-retaining mechanisms account for the structure-dependent stability in the ORR and play cornerstone roles in formulating ORR core-shell electrocatalysts.

1. Introduction

Stabilizing the oxygen reduction reaction (ORR) electrocatalysts over a long operating term is a fundamental issue for fuel cells and metal-air batteries.[1-5] This requirement is peculiarly important for Pt-based multimetallic nanocrystals as such ORR electrocatalysts are considered to fairly reduce our dependence on platinum—a scarce, expensive source—toward the development of those electrochemical energy frameworks.[6-11] Indeed, the US Department of Energy (DOE) specified the target of the 5000-hour lifetime for the Pt-based ORR electrocatalysts.[12] Upon catalyzing the ORR, nanocrystal electrocatalysts such as the standard Pt/C undergo the cycling of dissolution and deposition, causing the particles to merge into larger ones and/or migrate to the electrolyte membrane.[1,5,13-15] Hence, the mass activity degraded as a consequence; examples include a voltage loss of fuel-cell powered vehicles in stop-and-go driving.[4]

Of particular interest is the Pt monolayer (Pt_{ML}) electrocatalysts comprising an atomic layer of Pt on a metal core, prepared by the galvanic replacement of an underpotentially deposited (UPD) Cu monolayer,[16] which we found as the most active catalyst in the long-term ORR.[10,11,17] The Pt_{ML} electrocatalysts represent one of the best ORR electrocatalysts and have aroused intensive interest leading to industrial scale-up production.[18,19] The Pd-Pt_{ML} core-shell electrocatalysts are most promising in terms of cost-effectiveness.[20] However, our earlier membrane electrode assembly (MEA) measurements showed the substantial loss of the Pd core during the 100k-cycle stability test.[10] Although theoretical calculations and synchrotron-based *in situ* characterizations demonstrated that the Pd dissolution can improve the stability of the Pt_{ML} shell,[10,21] such loss

of inner cores must be circumvented prior to practical applications of these core-shell catalysts not only to reduce the cost but also to sustain the functions of the membrane and the two electrodes. These outcomes require a systematical study on the ORR stability of the Pt_{ML} electrocatalysts to comprehensively understand the driving forces to change their composition and components in the core-shell electrocatalysts, and solutions to stabilize the electrocatalysts themselves. However, MEA measurements were limited to the studies of the initial and end states of the electrocatalysts. The dynamic evolution in their structure during the ORR as well as the driving forces governing the dissolution of Pd are elusive. More importantly, these measurements on a whole cell lack adequate evidence to accurately reflect the performance of the ORR electrocatalyst, because the whole-cell output is influenced by many more factors than the electrocatalyst, such as degradation of the polyelectrolyte, deactivation of the anode electrode, and undefined mass transport conditions.[22] In addition, the essential reason for the ultra-high ORR stability of the Pt_{ML} electrocatalysts also warrants further investigation.

Without interference from the abovementioned limitation, the rotating disk electrode (RDE) technique with well-defined mass transfer provides a powerful measure to obtain true electrochemical reaction rates for fuel cell reactions.[23] In this communication, by combining the RDE technique with advanced structural characterization methods and model analysis, we described the interdependence of the electrocatalytic activity of the $Pt_{ML}/Pd/C$ catalyst on its structural evolution during the ORR. For the stability test up to 100k cycles, the catalyst displayed a volcano-like mass/dollar activity profile. Furthermore, we mapped the dynamic structural evolution of the Pd core and the Pt_{ML} shell during the reaction, and discuss the

4

core-shell interaction with respect to their sizes and structures. Through reliable and comprehensive study, a new mechanism for the ultra-high ORR stability of Pt_{ML} electrocatalysts is proposed.

2. Experimental

2.1 Chemicals and Materials

We purchased from Sigma the $CuSO_4$ (99.999% trace metals basis) and K_2PtCl_4 (99.99% trace metals basis), and Fisher Scientific supplied H_2SO_4 (optima grade) and $HClO_4$ (optima grade). Carbon-supported noble metal catalysts, *i.e.,* Pt/C (20 wt%, 4 nm) and Pd/C (20% by weight), were obtained from E-TEK division, PEMEAS Fuel Cell Technologies. We placed a Pt monolayer (Pt_{ML}) on the Pd/C to form Pt_{ML}/Pd/C, via the galvanic displacement with Pt of an underpotentially deposited Cu.[16] This synthesis was conducted by a procedure reported previously in a home-made, two-compartment electrochemical cell. All the aqueous solutions were prepared in 18 MΩ cm Milli-Q UV plus deionized water.

2.2 Materials Characterization

The components and composition of the electrocatalysts before and after stability test of different cycles were determined by a combination of X-ray photoelectron spectroscopy (XPS, Thermo Fisher Scientific-ESCALAB 250Xi) and energy dispersive X-ray spectroscopy (EDX) built-in FEI Helios Nanolab 600i field-emission scanning electron microscope (SEM). Transmission electronic microscopy (TEM) images were taken with a TecnaiG2F30 TEM operating at 300 kV. The scanning transmission electron microscopy (STEM) and electron energy-loss spectroscopy (EELS) measurements were performed with the dedicated aberration-corrected STEM (Hitachi HD-2700C) coupled with a modified Gatan Enfina ER

spectrometer. In addition, a cuboctahedral model was employed to further analyze the composition and structure of the $Pt_{ML}/Pd/C$ catalyst (see Supporting Information for details).

2.3 Electrochemical Measurements

A 5-mm diameter glassy carbon electrode (GCE, Pine Instrument, USA) was used for electrochemical measurements. All the electrochemical measurements were carried out at room temperature (25 ^{o}C) with a three-electrode system consisting of an electrochemical workstation (CHI 604d, CH Instruments), a catalyst-loaded GCE working electrode, and a platinum-flag counter electrode. An Ag/AgCl (3M NaCl filled) reference electrode was used throughout the electrochemical measurements while all the potentials presented were cited against a reversible hydrogen electrode (RHE). The potential difference between the reference electrodes was calibrated daily in a H_2-saturated 0.1 M $HClO_4$ solution to ensure the good accuracy of the ca. potential values of the working electrodes. RDE voltammograms were recorded at the rotating speed of 1600 rpm with a potential scan rate of 10 mV s^{-1}, and the positive-going segment was used for determining the ORR kinetic current at 900 mV. The amount of Pt at the electrode was inferred by calculating the coulombic charge of a UPD copper monolayer. We obtained the values of the electrochemical surface-area (ECSA) by integrating the hydrogen adsorption peak over time in the cyclic voltammograms (CV), referring to 210 μC cm$^{-2}_{ECSA}$.[24]

The accelerated degradation test (ADT) was conducted in air-saturated 0.1 M $HClO_4$ by subjecting the electrodes to potential scanning from 0.65 to 1.05 V at the scanning rate of 50 mV s^{-1}, viz. similar to the operating conditions in stop-and-drive vehicles.[4] We studied 100k cycles for the degradation test wherein electrochemical measurements were carried out every

10k cycles in freshly-prepared 0.1 M HClO$_4$ after cleaning the electrodes with deionized water.

3. Results and Discussion

3.1. ORR activity of Pt$_{ML}$/Pd/C

We prepared the Pt$_{ML}$/Pd/C electrocatalyst according to our previous Cu UPD pathway (Figure S1), and elucidated the difference in electrochemical properties by comparing the CVs of Pt$_{ML}$/Pd/C, Pt/C and Pd/C. The blue-, green-, and red-curves shown in Figure 1a represent the typical CVs of the Pt$_{ML}$/Pd/C, the Pd/C, and the Pt/C, respectively, which were obtained in an Ar-saturated 0.1 M HClO$_4$ at a scan rate of 50 mV s^{-1}. The Pd/C and Pt/C particles both exhibited two distinct peaks in the potential range of +0.05 V ~ +0.40 V pointing to the respective facet-specific UPD of hydrogen. In contrast, the UPD of hydrogen at the Pt$_{ML}$/Pd/C produced a facet non-specific peak at around +0.15 V, implying that the surface Pt atoms might be arranged on the Pd/C in the same way. Noticeably, its peak positioned between those of the Pd/C and the Pt/C. This observation can be related to the Pd-Pt core-shell interaction that modified the electrochemical properties of the surface Pt. On the other hand, the same core-shell interaction was evidenced by comparing the surface oxidation and reduction in the range of +0.6 V ~ +1.0 V. As shown in Figure 1a, at the Pt$_{ML}$/Pd/C, the commencing surface oxidation was shifted to a more positive potential than the Pd/C; but it still was obviously more negative compared with that of Pt/C. However, the corresponding cathodic responses showed that, at the Pt$_{ML}$/Pd/C, the adsorptive oxygen desorbed the fastest among these three catalysts, as evidenced by its most positive reduction peak with the greatest integral of Faraday current over time. This anodic and cathodic

procedure seemed inconsistent in terms of the surface oxygen binding energy. This counter-intuitional inconsistence may be related to an incomplete coverage on the Pd core by the Pt monolayer wherein the uncovered Pd is preferentially oxidized. However, the most positive reduction peak at the $Pt_{ML}/Pd/C$ corresponded to the relatively weakened binding to surface oxygen.[25] This feature will accelerate the renewal of surface active sites and thus improve the ORR kinetics.
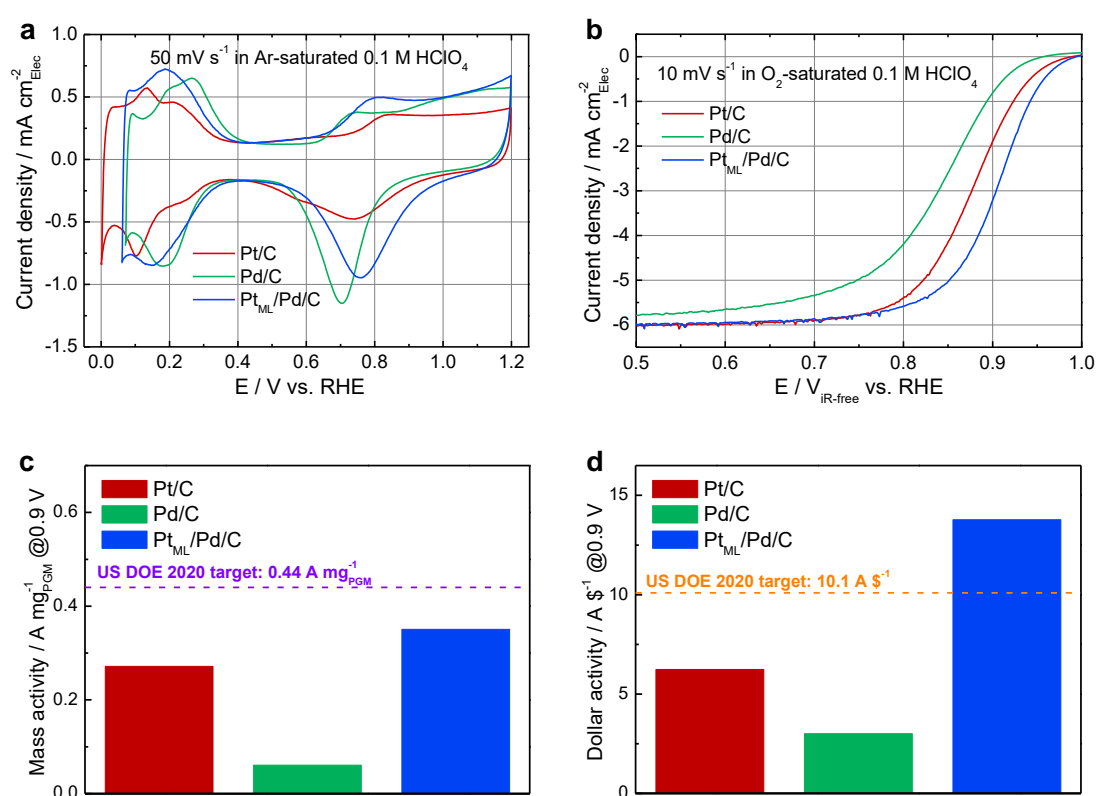
Figure 1. (**a**) Cyclic voltammetry curves (50 mV s^{-1}) and (**b**) ORR polarization curves (10 mV s^{-1}, 1600 rpm) of E-TEK Pt/C, E-TEK Pd/C, and $Pt_{ML}/Pd/C$ with the loadings of 10.2 μg_{Pt} cm^{-2}, 15.3 μg_{Pd} cm^{-2}, and 19.7 $\mu g_{(Pt+Pd)}$ cm^{-2}, respectively, recorded in a 0.1 M HClO$_4$ solution. And their corresponding (**c**) mass and (**d**) dollar activities at a potential of 0.9 V, respectively.

To start with, we examined the influence of the Pt monolayer in the $Pt_{ML}/Pd/C$ on its ORR kinetics by comparing its polarization curve to the Pd/C and the Pt/C. Shown in Figure 1b are the blue-, green-, and red-curves that, respectively, represent the typical *iR*-free polarization curves of the $Pt_{ML}/Pd/C$, the Pd/C, and the Pt/C, acquired in the O$_2$-saturated 0.1 M HClO$_4$

solution at a scan rate of 10 mV s^{-1} by using the RDE technique. The Pt$_{ML}$/Pd/C exhibited a half-wave potential ($E_{1/2}$) 65 mV higher than Pd/C and, more remarkably, even much greater than Pt/C. This highest value of $E_{1/2}$ of the Pt$_{ML}$/Pd/C highlighted the essential role of its Pt monolayer that dramatically improved the apparent ORR kinetics. Furthermore, we calculated its platinum group metal (PGM) mass activity of 0.35 A mg$^{-1}_{PGM}$ using the *Koutecký-Levich* Equation as shown in the histograms in Figure 1c to compare with the values obtained for the Pd/C and the Pt/C, and the 2020 target of US DOE.[12] The same increasing trend was true for the specific activity (Figure S2), with the Pt$_{ML}$/Pd/C being the most active electrocatalyst. It is worth noting that the PGM mass and specific activities of the catalyst in this study are higher than in our earlier publications (refs. 26&27). The higher values of mass- and specific-activity for both the Pt/C and Pt$_{ML}$/Pd/C electrocatalysts in the present study can be attributed to the correction of the uncompensated *iR*-drop caused by solution resistance. Recent studies have demonstrated the advantages of *iR*-correction to obtain a reliable result for ORR measurement in three-electrode system.[28] In addition, it is important to notice that the monolayer-achieved activities actually remained somewhat lower than the US DOE target. Interestingly, these activities, if normalized by the price of PGM (see Figure S3), appeared to be much higher than the US DOE target (Figure 1d). Indeed, the dollar activity was recently proposed for convenience to evaluate the ORR activity of such materials,[29] since multi-component, noble metal-containing crystals have been the subject of tangible studies of formulating ORR catalysts. Considering the difference in price/cost between different noble metals, this proposal is reasonable when targeting their practical applications in commercializing fuel cells, although the dollar activity also does not

accurately quantify their production cost. Hence, our choice of Pd to replace the inner Pt was not only based on the favorable Pd-Pt core-shell interaction but also the relative inexpensiveness and abundance of Pd (only about half the price of Pt, and 200 times more in reserves than Pt[30]).

3.2 ORR activity and structural evolution of Pt_{ML}/Pd/C in stability test

On the basis of the latest protocol of US DOE,[12] and considering the difference in RDE electrodes and MEAs, we used slightly more accelerated conditions (i.e., potential-scanning window of 0.65 to 1.05 V *vs*. 0.60 to 0.95 V (DOE)) to interrogate the stability of the Pt_{ML}/Pd/C within 100k-cycle test while including the counterpart results of the Pt/C as reference (Figure 2). We calculated the dollar activities and the specific activities based on the corresponding polarization curves (Figures S4&S5). The Pt/C registered up to 28% loss of the initial dollar activity in 30k cycles of the stability test. This degradation was related to the particle-size increasing of Pt in the Pt/C during the potential scanning, namely electrochemical Ostwald ripening, therefore lowering the utilization of Pt.[1,5,13-15] Unlike the Pt/C, at which the dollar activity descended linearly, the activity of the Pt_{ML}/Pd/C evolved in a volcano-like trend—that is, it increased by 10% in the initial 20k cycles and then dropped to 83% of the initial value at the end of the stability test. Furthermore, all the dollar activities were higher than the DOE target throughout the 100k-cycle test, indicating the excellent stability of this electrocatalyst as demonstrated in MEA measurement. In addition, it can be expected that since the amount of PGM in Pt_{ML}/Pd/C electrocatalyst loaded on the electrode and the cost of these PGM correspond to each other, the PGM mass activity of Pt_{ML}/Pd/C exhibited the same volcano-like profile with the dollar activity, so did its Pt mass activity.

Figure S6a&b shown that the PGM mass and Pt mass activities of $Pt_{ML}/Pd/C$ increased from the initial 0.35 A mg^{-1}_{PGM} and 1.57 A mg^{-1}_{Pt} to 0.39 A mg^{-1}_{PGM} and 1.72 A mg^{-1}_{Pt}, respectively, after 20k potential cycles. Besides, in our previous total 15k-cycle stability test, the ORR activity enhancement of $Pt_{ML}/Pd/C$ was also observed.[27] This counterintuitive observation seemed yet reasonable because the inner Pd core was relatively unstable so as to be dissolved preferentially, enabling stabilization of the surface Pt. Concurrently, the loss of the core induced re-arrangement of Pt atoms toward a higher-coordination, more stable configuration. Recent studies have demonstrated that the ORR acidity is higher on the higher coordinated Pt sites.[31,32] The structure-dependent stability of $Pt_{ML}/Pd/C$ catalyst in the ORR will be further discussed in more detail with experimental and calculated results.
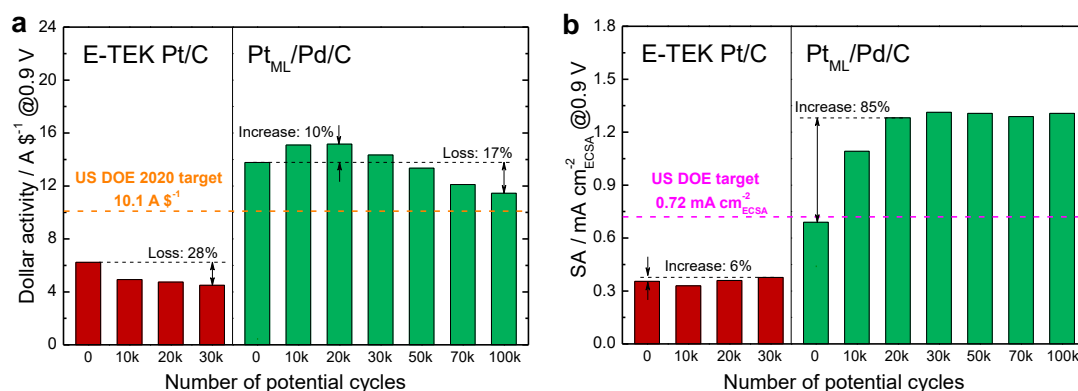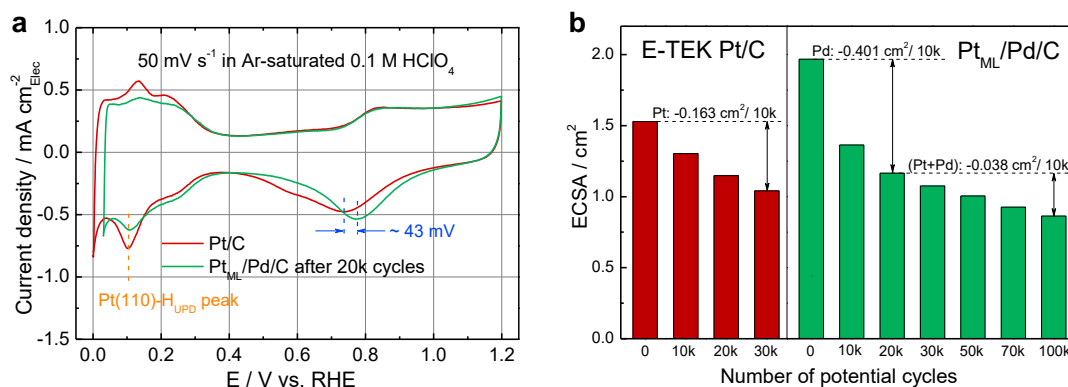

Figure 2. (**a**) Dollar activities and (**b**) specific activities of E-TEK Pt/C and $Pt_{ML}/Pd/C$ at 0.9 V as a function of the number of potential cycles (0.65 ↔ 1.05 V) during the ADT.

Figure 2b shows the histograms of the specific activities of the $Pt_{ML}/Pd/C$ and Pt/C electrocatalysts for the ORR after different cycles of the stability test. Interestingly, the 20k-cycle stability test caused the $Pt_{ML}/Pd/C$ to increase its specific activity by as high as 85 %, an order of magnitude greater than did the Pt/C (6 %), although the overall increasing trend was true for both cases. This remarkable difference underscored the Pd-Pt core-shell interaction that enabled the surface Pt atoms to re-arrange themselves to the most optimal

11

geometric and electronic configuration for the ORR. For the Pt/C, the particle-size increased throughout the stability test lowering the fraction of surface defect sites such as the low-coordinated edge- and vertex-atoms, which was accredited with improving its specific activity.[31,32] To the contrary, for the Pt_{ML}/Pd/C, the first 20k-cycle stability test induced decreasing of the particle size (see below) as Pd atoms exposed at defects or voids in Pt_{ML} dissolved due to its relatively low corrosion resistance, such that the Pt atoms could remain on the surface and shrink into a contiguous, highly coordinated atomic layer. In the subsequent stability test over 20k cycles, its specific activity increased with a dramatically reduced rate that was comparable to that for the Pt/C, pointing to the increase of the particle size due to electrochemical Ostwald ripening. As seen in Figure S4a&S5a, the changes in voltammetric behavior of Pt_{ML}/Pd/C from 20k to 100k cycles are similar to those of Pt/C from initial to 30k cycles.

To gain insight into the electrochemically-induced evolution of the surface state, we compared the representative CV of the Pt_{ML}/Pd/C after 20k-cycle stability test to that of the freshly prepared Pt/C, and their corresponding ECSAs that we calculated by integrating the Faradic current of the hydrogen UPD. Careful review of the curves (Figure 3a) suggests a comparable voltammetric behavior, particularly the facet-specific hydrogen UPD peaks on Pt (highlighted as Pt(110) in Figure 3a), denoting that a monolayer of Pt atoms compactly stacked side-by-side on the surface of the Pt_{ML}/Pd/C. Also shown therein is the reduction peak at around 0.78 V, viz. 43 mV higher than Pt/C, which we designated to the relatively much fast dissociation of oxygen at the Pt_{ML}/Pd/C.[25] Taken together, these electrochemical results demonstrated the evolution of a nearly ideal Pt monolayer that interacts with the Pd

core to acquire modified electronic- and electrochemical-properties. In other words, the original Pt monolayer prepared by the UPD technique might be loosely stacked within the Pt atoms and have low coordination with the underpinning Pd atoms. Therefore, the dissolution of Pd atoms during the stability test induced the re-arrangement of surface Pt atoms, and the formation of a highly-coordinated, contiguous Pt monolayer. As this process undergo, the inner Pd core evolve into smaller particles until it was fully encompassed by the as-formed Pt monolayer. This self-healing feature fundamentally differ from the subsequent Ostwald ripening, as evidenced by the relatively insignificant and/or slow change in CVs and ECSAs over 20k cycles. To justify, we evaluated the rate of the ECSA loss before and after 20k cycles, respectively (Figure 3b). For the last 80k cycles, we calculated an ECSA-loss rate of 0.038 cm^2 per 10k cycles that was ten times lower than the value of the initial 20k cycles. Not only this, but the ECSA-loss rate of Pt_{ML}/Pd/C during 20k-100k potential cycles was also significantly lower than that of the standard Pt/C (0.163 cm^2 per 10k), indicating that the Ostwald ripening kinetics of Pt_{ML}/Pd/C is slower, which accounts for its excellent stability. In addition, the corresponding Pt-mass specific ECSAs (ECSA normalized to the Pt mass on the electrode) of Pt_{ML}/Pd/C during stability test are also calculated for further evaluation. It can be seen from Figure S7 that in the initial stage, the Pt_{ML}/Pd/C electrocatalyst (227 m^2 g^{-1}_{Pt}) exhibited three times higher Pt-mass specific ECSA than the Pt/C (76 m^2 g^{-1}_{Pt}); moreover, it still remains an ECSA of 100 m^2 g^{-1}_{Pt} after 100k-cycle stability test, indicating a high Pt utilization in long-term ORR.

13

Figure 3. (a) Cyclic voltammetry curves of the initial E-TEK Pt/C and the Pt_{ML}/Pd/C after 20k-cycle ADT, respectively, measured with a scan rate of 50 mV s^{-1} in Ar-saturated 0.1 M HClO$_4$. (b) ECSAs of E-TEK Pt/C and Pt_{ML}/Pd/C as a function of the number of potential cycles (0.65 ↔ 1.05 V) during the ADT.

Combining EDX and XPS (Figures S8&S9) analyses to acquire dynamic information of the particles' composition throughout the stability test, we summarized in Figure 4 the changes in Pd-atomic portion with respect to potential cycles. Our EDX and XPS analyses produced a consistent descending trend over all the measurements. XPS measurements gave rise to the relatively lower values; however, this observation was fairly comprehensive because the intrinsic energy density of x-ray beam-line and inelastic mean free path of escaped electrons determined the limit of detection of ~1.5 nm depth.[33] Hence, this difference agreed with the Pd-Pt monolayer core-shell structure. Further, the EDX results exhibited an overall loss of the Pd but significantly more than 57% Pd remains after 100k cycles highlighting the protection function of the Pt monolayer covering. More importantly, like the ECSA change shown in Figure 3b, close analyses of Figure 4 reveal a similar dramatic difference in the rate of losing Pd atoms before and after the 20k-cycle stability test. Indeed, the surface-sensitive XPS results suggested 8.9% per 10k cycles from the beginning to the 20k cycle, which was much greater than the subsequent stability test (1.7% per 10k cycles). We confirmed that the initial 20k-cycle stability test achieved a nearly ideal Pt monolayer

efficiently enough to retard the loss of the Pd core. In addition, no oxidation state of Pd was observed in the Pd3d XPS spectra of Pt_{ML}/Pd/C after 20k to 100k cycles also indicated the Pd atoms in the cores were effectively protected (Figure S9a). Noticeably, the subsequent Ostwald ripening during 20k-100k potential cycles of the Pt_{ML}Pd/C was a little different from the case of Pt/C. Actually, both Pt and Pd atoms were dissolved slowly, although the Pd core-full covered Pt shell structure were always remained in the Pt_{ML}Pd/C.
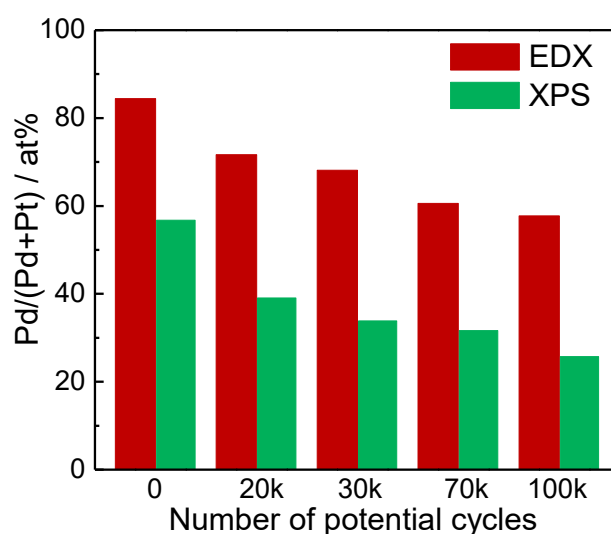
Figure 4. The Pd/(Pd+Pt) atomic ratio of Pt_{ML}/Pd/C electrocatalyst as a function of the number of potential cycles (0.65 ↔ 1.05 V) during the ADT determined by EDS and XPS measurements, respectively.

Z-contrast high-angle annular dark field (HAADF)-STEM images and corresponding EELS mappings of Pt from Pt_{ML}/Pd/C before and after 20k cycles and 100k cycles are shown in Figure 5. The Pt shell thickness, which was roughly estimated from the EELS mappings in the figure, is 0.42 nm, 0.48 nm, and 0.70 nm before and after 20k cycles and 100k cycles, respectively. The Pt shell thickness apparently increases with an increase of the number of potential cycles; particularly the increase in shell thickness after 100k cycles compared with that before cycling is prominent. Although it is quite difficult to determine the exact thickness from the STEM-EELS data and a statistical approach is necessary for further analyses.

15
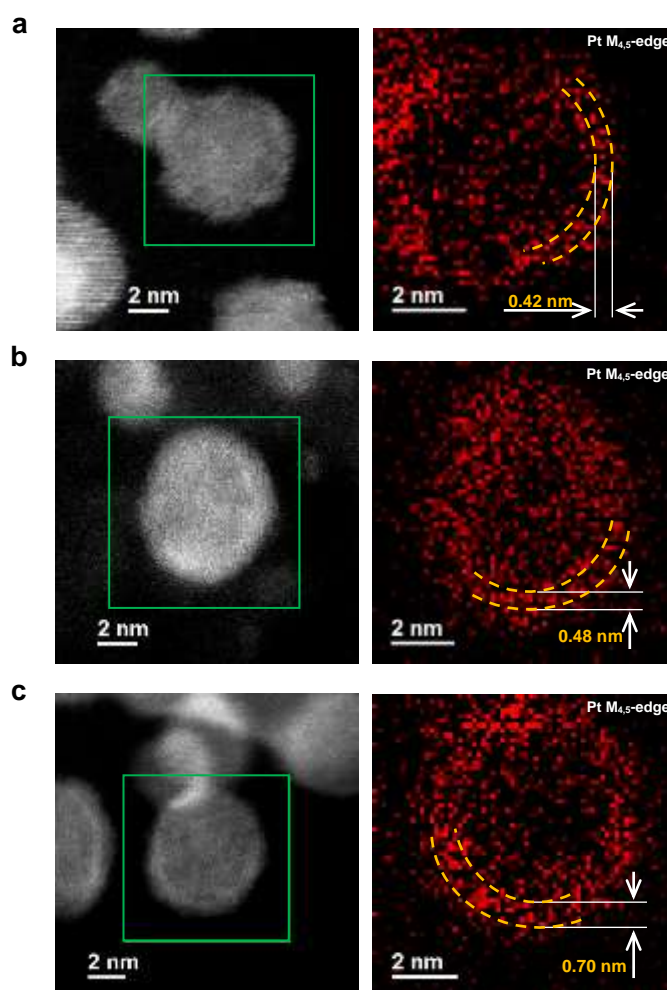
Figure 5. Z-contrast HAADF-STEM images of single nanoparticles and their corresponding 2D STEM-EELS maps of Pt obtained with 0.13 nm/pixel resolution. (**a**) Initial Pt_{ML}/Pd/C; (**b**) Pt_{ML}/Pd/C after 20k cycles; (**c**) Pt_{ML}/Pd/C after 100k cycles.

The particle size distributions before, and after 20k and 100k cycles are depicted in Figure 6, and the mean diameters of the nanoparticles are determined to be 6.4 nm, 5.3 nm, and 6.7 nm, respectively. Interestingly, the particle size first decreases after the 20k cycle test, and then increases after the 100k cycle test. As discussed later, during the initial 20k cycle test, exposed Pd atoms of the core dissolve away, thereby inducing slight shrinkage of the particle size with relaxation of the Pt shell. On the other hand, an increase in particle size after the 100k cycle test can be explained by electrochemical Ostwald ripening. The notion is also supported by STEM observations shown in Figure 7. STEM images of the Pt_{ML}/Pd/C catalyst

16

after the 100k test show round-shaped particles with a much more uniform size distribution, while those of initial $Pt_{ML}/Pd/C$ show various shapes of particles with a wider size distribution. Smaller particles in the initial catalyst may have been dissolved and redeposited on larger particles. Such the observation in size distribution is coincident with a decrease in standard deviation in particle size distribution after the 100k cycle test (0.80 nm) compared with those before and after the 20k cycle test (1.00 nm). In general, smoother and reduction of low-coordinated Pt surfaces increase the ORR activity.[31,32] Such effect may be operative in the present system; however, we consider that the activity degradation due to the increase in particle size during the repetitive 100k potential cycling is more dominant, as discussed in details later.
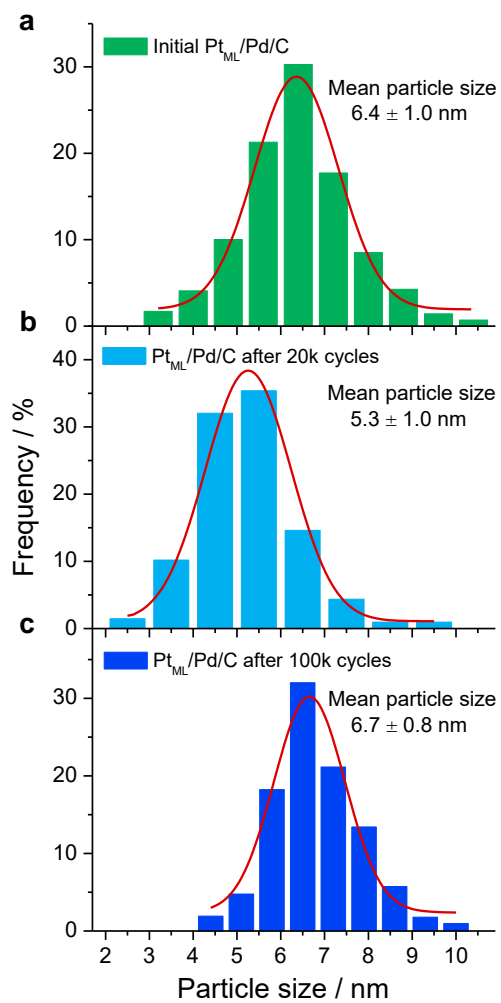
Figure 6. Particle size distributions of **(a)** initial Pt$_{ML}$/Pd/C, **(b)** Pt$_{ML}$/Pd/C after 20k cycles, and **(c)** Pt$_{ML}$/Pd/C after 100k cycles.
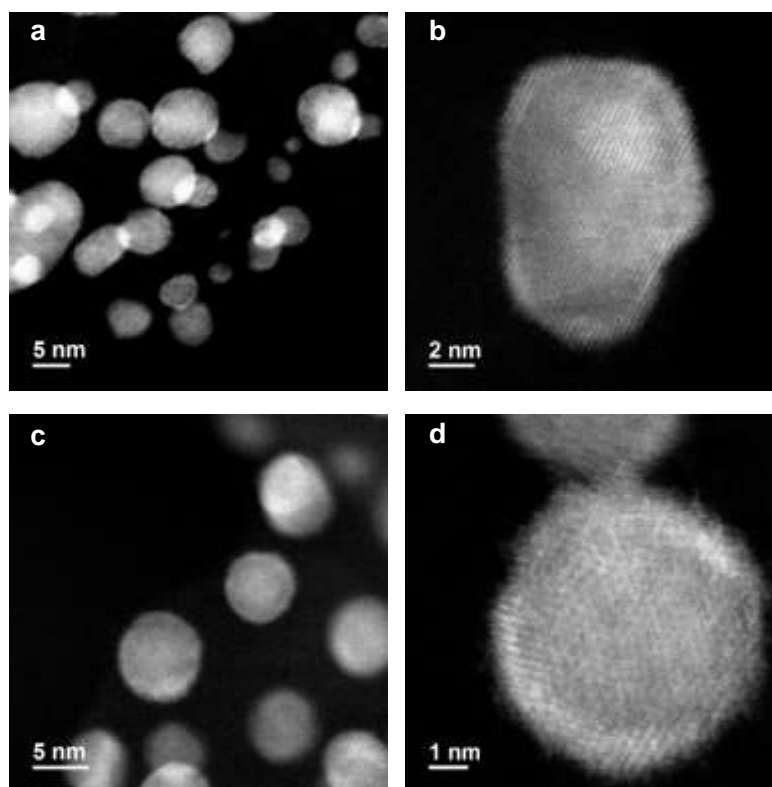
Figure 7. Z-contrast HAADF-STEM images of (**a**, **b**) initial $Pt_{ML}/Pd/C$ and (**c**, **d**) $Pt_{ML}/Pd/C$ after 100k cycles.

3.3 Model analyses of structural- and compositional-evolution

Above experimental results demonstrated that the Pt monolayer prepared by the UPD and galvanic replacement techniques comprised fragmental atomic layers that were structurally discontinued and electrochemically unstable. To advance the understanding of the structure and composition of the $Pt_{ML}/Pd/C$, and their evolution during the stability test, a regular polyhedron mode with a close-packed crystal structure was chosen as our starting Pd/C crystal to simulate the growth of supported Pt monolayer and the change of the entire nanostructure. For the simplest optimal Pd(100) and Pd(111) surfaces of Pd single crystals, the global-minimal-energy principle predicted that Cu atoms can be under-potentially deposited on the four-fold and three-fold hollow sites (denoted as F sites and T sites),[34,35] respectively, as illustrated in Scheme 1a. Consequently, the UPD Cu layer consisted of the

same atomic number as that of the outmost Pd layer, corresponding to the electric quantity of

0.421 mC$_{Pd(100)}$ and 0.486 mC$_{Pd(111)}$ per centimeter square,[36] given that the hollow sites were

in the same amount as the sublayer atoms.
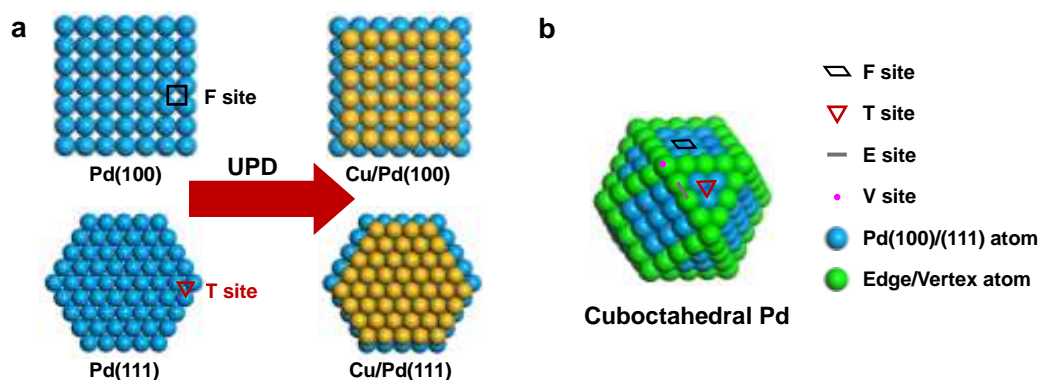
Scheme 1. (**a**) The model of Pd(100) and Pd(111) single crystals and the Cu-UPD on the respective model surfaces. (**b**) The cuboctahedral Pd model. The corresponding surface sites and surface atoms were marked.

Real-world Pd nanostructures (e.g., cuboctahedral particles, as shown in Scheme 1b) comprise much more complicated surfaces than the ideal single crystals; in addition to the Pd(111) and Pd(100) facets, on the particles' surface there are defect sites, including inter-planar edges and vertexes (denoted as E sites and V sites, respectively).[31] We employed the nanoscaled cuboctahedron model to illustrate the growth and state of a Pt monolayer. Calculations for such nanoparticles of varied sizes are tabulated in Table S1. We shall discuss the portion of surface Pd atoms and the corresponding coverage by Pt, assuming two different situations: Cu UPD occurred on the entire surface and on F- and T-sites only. In both situations, we assumed that all the UPD Cu atoms were displaced with Pt in the same mole amount. More details on the model analyses can be found in the Supporting Information. Figure 8a shows the change of the portion of surface Pd atoms of a cuboctahedral particle, and the portion of F- and T-sites among all the surface atoms, with the particle size being

varied from 0.274 nm (one atom) to 10.06 nm ($v = 21$). Noticeably, as the particle size increase, the ratio of the surface atoms to the total descended while the ratio of the F- and T-sites to the total surface atoms ascended. For the size of 6 nm, the surface atoms accounted for 21.6%, among which there were 81.3% atoms comprising F- and T-sites. Figure 8b shows the corresponding surface coverage by Pt of the cuboctahedral particle. We observed a similar increasing trend with or without the edge/vertex sites being considered. Noticeably, the coverage remained less than 100% for all the particles and so caused certain Pd atoms to be electrochemically corrosive. This adverse situation was even worse, considering that Pt, a more inert metal, could prompt the corrosion of Pd. This observation seemed understandable because a full covering of Pt on Pd particles required the atomic number greater than that of the surface Pd. For the case of the layer number of 12 (Pd size, ~5.9 nm), the surface Pd atoms was calculated to be 1442, that is, the difference of the total atomic numbers between the layer numbers of 11 and 12 (Table S1). Likewise, we calculated the number of Pt atoms of 1692 that was required for a full covering on this Pd particle. Since the Cu UPD technique can produce a Pt monolayer consisting of maximal 1442 atoms, limited by the surface Pd, the ideal coverage was 85% (i.e., 1442/1692) (Figure 8b). This value was even lower when excluding the Cu UPD on the E- and V-sites. In this context, the uncovered surface Pd was subjected to electrochemical corrosion during the stability test until the particle size shrunk to the same as that of the one-less layer number, such that the Pt protecting layer could fully cover the Pd core.
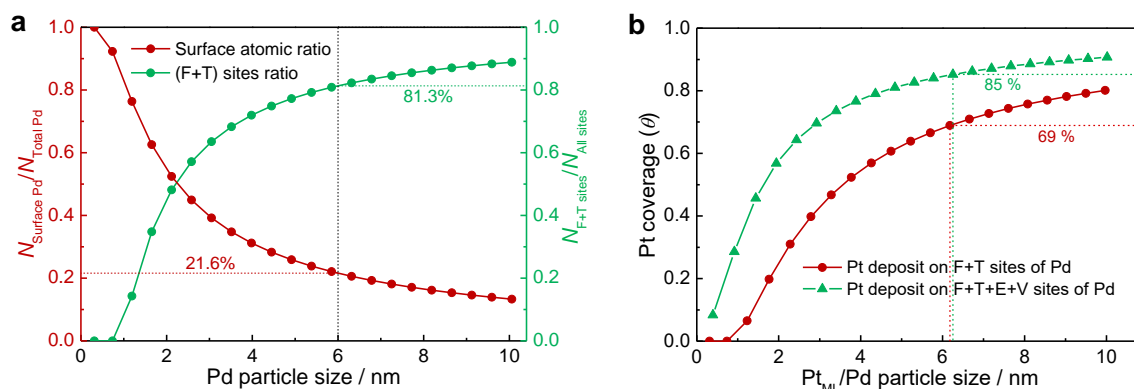
Figure 8. (**a**) The numeric ratio of the number of surface atoms to the number of total Pd atoms (red curve), and the numeric ratio of the sum number of F- and T- sites to the sum number of F-, T-, E-, and V- sites (green curve) as a function of the Pd particle size, respectively. (**b**) the Pt coverages in the cases of Cu UPD on all F-, T-, E-, and V- sites and Cu UPD on only F- and T- sites, respectively, as a function of the Pt_{ML}/Pd particle size.

On the basis of the self-healing property, and assuming negligible loss of Pt (cathodic protection[10]), we further envisaged the changes of surface area, particle size and Pt/Pd atomic ratio for these two cases of Cu UPD. This assumption corresponded to our first 20k-cycle stability test only, because the electrochemical results suggest that the undissolved Pd atoms are just covered fully by Pt atoms at the $20k^{th}$ cycle (Figure 3). The solid curves in Figure 9a show the surface area loss of the Pt_{ML}/Pd of different sizes, with Cu UPD occurring on all sites (triangled) and on the F- and T-sites only (circled). We observed a remarkable difference of 0.1 or greater for all the studied particle sizes, indicating a relatively high surface area loss for the case of Cu UPD on F- and T-sites alone. Also included in Figure 9a are the particle sizes of the Pt_{ML}/Pd, with a full Pt covering after the completion of the Pd loss, in relation to that of its original form. Apparently, the site-selective Cu UPD resulted in more significant shrinking in the diameter (hollow circled), agreeing with the experimental ECSA loss. As the particle size increased, the change of particle size to realize a full Pt covering became closer to one another because of size-determined fraction of edge and vertex sites (Figure 8a).

Accordingly, for these site-selective and non-selective cases of Cu UPD, we plotted in Figure 9b the atomic Pt-to-Pd ratio before and after the formation of the full Pt covering. For the site-selective Cu UPD, the change of the Pt portion, viz. the difference between the two red curves at a specific particle size, was essentially greater than the non-selective Cu UPD. Combining these calculated results, we concluded that increasing the Pt_{ML}/Pd particle size reduced the loss of Pd until the formation of a full covering of Pt monolayer; and this was particular true for the case of Cu UPD on all the surface sites. Furthermore, for the Pd particles of 6 nm that we used in our experiments (TEM image and particle-size distribution are shown in Figure S10), the calculated results are tabulated in Table 1 in parallel with the experimental observations. Comparison indicates that the site-selective mode of the Cu UPD (i.e., on F- and T-sites alone) are the likely approach what practically occurred in our experiments. The calculation-to-experiment discrepancy implied more complicated situations that could induce the loss of Pd, including non-*in situ* replacement with Pt of Cu atoms and thus the formation of Pt clusters. For instance, calculations for 6 nm particles revealed the maximal coverage of 69% (Figure 8b) in the case of Cu UPD on F- and T-sites only; however, the corresponding electrochemical experiments showed the ECSA dropping from 1.97 cm^2 to 1.17 cm^2, viz. 40.7% loss, indicating the coverage of 59.4% (1.17/1.97) in our experiments. Therefore, the difference of 10% is most likely due to the formation of Pt cluster or Pt bilayer.
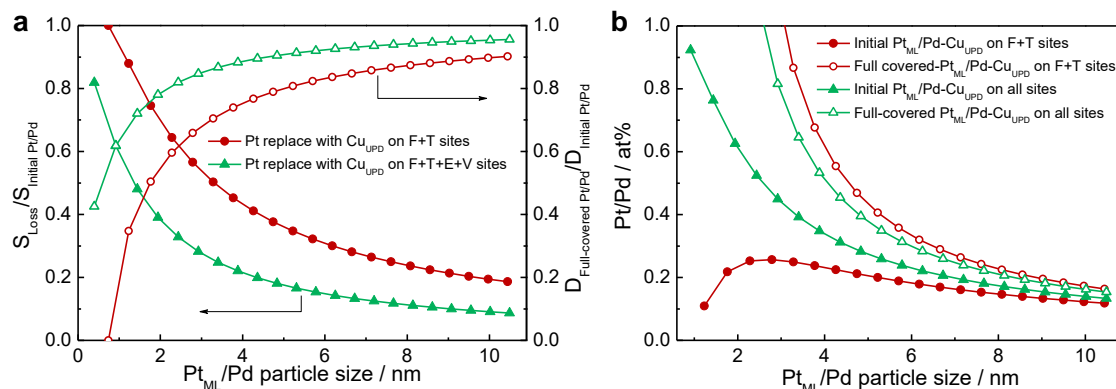
Figure 9. (**a**) Surface area loss (solid) and particle size change (hollow) before and after self-healing as a function of the initial Pt_{ML}/Pd particle size. (**b**) The Pt/Pd atomic ratio of in the initial Pt_{ML}/Pd particle to in the full-covered Pt_{ML}/Pd particle, respectively, as a function of the initial Pt_{ML}/Pd particle size. The curves of both of the Cu UPD cases were plotted.

Table 1. Comparison of the calculated results from model analyses with experimental results.

|	Model analyses		Experiments
	$Pt_{(F+T+E+V)}/Pd$	$Pt_{(F+T)}/Pd$	$Pt_{ML}/Pd/C$
Initial particle size (nm)	6.41	6.33	6.4 nm[a]
$D_{Full-covered\ Pt/Pd}/D_{Initial\ Pt/Pd}$	93%	84%	83%[b]
Initial Pt/Pd atomic ratio	21.6%	17.6%	18.4%[c]
Full-covered Pt/Pd atomic ratio	27.5%	31.1%	39.5%[d]
$S_{Loss}/S_{Initial}$	13.9%	29.5%	40.7%[e]

Notes: [a] STEM result of the initial $Pt_{ML}/Pd/C$ (Figure 6a). [b] STEM result of the $Pt_{ML}/Pd/C$ before and after 20k cycles (Figure 6a&b). [c] EDX result of the initial $Pt_{ML}/Pd/C$ (Figure S8a). [d] EDX result of the $Pt_{ML}/Pd/C$ after 20k cycles (Figure S8b). [e] ECSA-H_{UPD} ratio of the initial $Pt_{ML}/Pd/C$ and the $Pt_{ML}/Pd/C$ after 20k cycles (Figure 3b).

3.4 Self-healing and Self-retaining mechanisms

Our experimental and calculated results demonstrated that Cu UPD can most likely take place on well-shaped Pd(111)- and Pd(100)-facets, instead of the edge or vertex sites of Pd nanoparticles. The Pt monolayer in the Pt_{ML}/Pd, formed by the galvanic replacement with Pt of the under-potentially deposited Cu monolayer, was actually a disconnected Pt submonolayer (sML) with relatively low theoretical-coverage, (e.g., 69% coverage for 6 nm Pd). In addition, non-*in situ* replacement with Pt of Cu-UPD, as mentioned above, contributed to lowering the Pt coverage, inducing the formation of defect sites like puncture

in each separated Pt layers, and/or exposing the Pd(111)- and Pd(100)- atoms to the electrolyte. Therefore, in the initial 20k-cycle stability test, the exposed Pd of the core dissolved out, inducing the shrinking and relaxing of the surface Pt, so forming a near-ideal Pd-Pt monolayer core-shell structure. The decrease in particle size after the 20k cycle test is clearly illustrated in Figure 6. This self-healing property of Pt monolayer electrocatalysts is slightly different from what was reported in our earlier review (ref. 37), which only highlighted the stabilizing effect of Pd-core dissolution on the Pt_{ML} shell. And we speculated previously that a fully-covered Pt_{ML} may not be formed during the ORR.[10,37] However, current results demonstrate that the initial incomplete Pt_{ML} can be self-healed. We consider that the relatively slow electrochemical-corrosion rate of core metal is the key to successful self-healing (i.e., from Pt_{sML} to Pt_{ML}).[38,39] It can guarantee enough time for the surface Pt to relax and reconstruct. For our Pt_{ML}/Pd/C electrocatalyst, the 20k cycle stability test achieved the nearly ideal core-shell structure. Afterward, the Pt_{ML}/Pd particles dissolved as a whole with a retarded kinetics; however, the core-shell structure remained throughout this process due to its structural self-retaining property. This self-retaining property specific to Pt_{ML} electrocatalysts is crucial to its long-term stability for ORR, we will further analyze the corresponding mechanism behind this feature below. Scheme 2 illustrates the dynamic structural evolution of the Pt_{ML}/Pd/C during the stability test, from a fresh structure prepared by the Cu UPD and galvanic replacement technique via a nearly ideal core-shell structure to a grown-up particle with a thicker Pt shell (2-3 MLs). As with the Pt/C, the increase in particle size of Pt_{ML}/Pd/C after 100k cycles is also as a result of the electrochemical Ostwald ripening. But the two Ostwald ripening processes are not identical. For the Pt_{ML}/Pd/C catalyst, after full

self-healing, the surface Pt atoms of a smaller $Pt_{ML}Pd$ particle are preferentially dissolved and redeposited on the surface of a larger $Pt_{ML}Pd$ particle during further stability test. Meanwhile, the exposed Pd atoms, caused by the dissolution of surface Pt atoms, will be dissolved. However, owing to the relatively lower reduction potential, the dissolved Pd is difficult to redeposit, as evidenced by the fact that no Pd signal can be found in the CV curves of $Pt_{ML}/Pd/C$ recorded during the 20k-100k-cycle stability test. Our previous MEA measurement showed that the dissolved Pd migrates to the Nafion membrane.[10] This special Ostwald ripening leads to increase the thickness of Pt shell of $Pt_{ML}/Pd/C$ during the 20k-100k-cycle test. It should be pointed out that the increase in Pt shell thickness of $Pt_{ML}/Pd/C$ would decrease the specific activity since the favorable interaction from the Pd core on the surface Pt atoms is weakened. On the other hand, the decrease in low-coordinated Pt atoms on the surface due to the particle growth would increase the specific activity. The relatively constant specific activities observed during 20k-100k cycles (Figure 2b) may well be caused by balancing these two opposing effects.
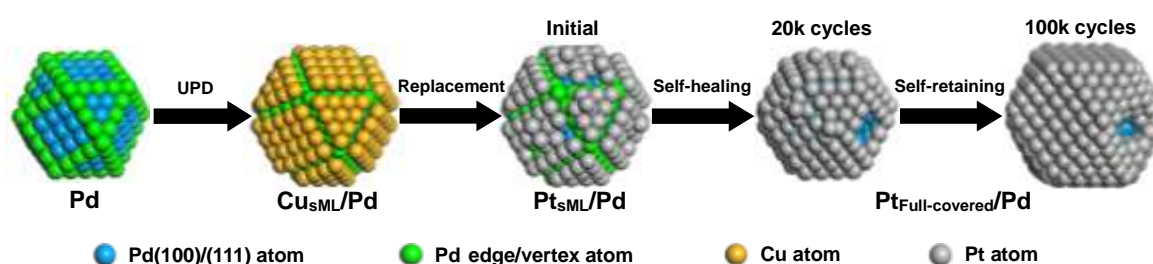
Scheme 2. Schematic illustrations of site-selective Cu UPD and then galvanic replacement with Pt on the surface of cuboctahedral Pd model, and the structural evolution of Pt/Pd particle during the stability test.

We also note that the present stability tests of the $Pt_{ML}/Pd/C$ catalyst were performed at a room temperature (25 °C). A recent study has shown that after an accelerated stability test of 10k potential cycles between 0.6 and 1.0 V at 80 °C a Pt/Pd/C core-shell catalyst showed

5-fold and 1.4-fold enhancements of specific activity and mass activity, respectively.[40] Stability tests of a 4-ML thick Pt on Pd(111) core-shell structure at 80 °C demonstrated that its durability under potential cycling depends on solution temperatures as well as upper potentials of the cycle tests.[41] The effect of solution temperatures on the stability of our Pt_{ML}/Pd/C catalysts is beyond the scope of the present study; however, in the near future we will investigate if a similar mechanism would be operational at higher temperatures. In order to better understand the structural self-retaining property of Pt_{ML} electrocatalysts, the structural change of the Pt bimetallic catalysts containing 3d-transition metals (Fe, Co, Ni, or Cu etc.) during the ORR has to be understood. For these catalysts, both the alloy structure and the core-shell structure (including the case of the Pt shell covered on a Pt alloy core) themselves are thermodynamically stable.[42,43] However, under the ORR conditions, whether alloy or core-shell the structure cannot retain for a long period due to the continuous surface segregation of 3d-transition metals from the interior of nanoparticles induced by the oxygen-containing species (i.e., OH_{ad}/O_{ad}) adsorbed on catalyst surface.[44-47] This phenomenon can be explained by the fact that the oxygen affinities of the 3d-transition metals are very different from that of Pt (theoretical calculations predict that the oxygen binding energies (ΔE_o) on Fe, Co, Ni, Cu and Pt are, in order, -0.90 eV，-0.22 eV，0.34 eV，1.20 eV and 1.57 eV[48]). This large difference in oxygen affinity can provide a powerful driving force to facilitate the 3d-transition metals surface segregation when oxygen-containing species are present on the catalyst surface, because these oxygen species are more willing to bind with the 3d-transition metals.[49,50] Once the transition metal atom reaches the surface, it will be rapidly dissolved out. As a result, its content decreased gradually, and ultimately changing

the alloy- and core-shell-structure of the Pt bimetallic catalysts. The change in structure will seriously weaken the electronic and lattice strain effects between Pt and 3d-transition metals, so the initially high ORR activity of these Pt bimetallic catalysts is difficult to maintain. The structural change of this kind of catalysts driven by adsorbate-induced surface segregation has already been the most important reason for the decay in its ORR activity during fuel cell operation.[51-53]

In contrast, for the $Pt_{ML}/Pd/C$, the difference in oxygen affinity between Pd and Pt is very small (ΔE_o of Pd surface is 1.53 eV,[48] which is only 0.04 eV difference from that of Pt.), moreover, the oxygen affinities of both Pt and Pt are relatively weak; hence, there is not enough driving force to facilitate Pd segregation from the inside to the surface, even if some oxygen-containing species adsorb on the catalyst surface. Density functional calculations have also shown that the Pd cannot segregate to the Pt surface under the ORR conditions.[49,54,55] In addition, it may also play a part role on the structural self-retaining of $Pt_{ML}/Pd/C$ catalyst that since the lattice between Pd and Pt is well matched (lattice mismatch is only 0.77%[56]). The interfacial stress between the Pd core and Pt_{ML} shell is very small, avoiding to form the lattice defects such as vacancies and dislocations at the interface, so that the Pt shell atoms can be evenly spread along the lattice of Pd core and play a better protective role to the Pd core. Our experimental work showed the major dissolution of Pd before the full self-healing, as evidenced by the loss of 53% Pd (calculated based on EDS results) in the initial 20k-cycle stability test. And the self-healed $Pt_{ML}/Pd/C$ exhibited a superior stability during the subsequent 80k cycles due to its unique structural self-retaining property. These findings enlightened us to develop fully-covered Pt monolayer

electrocatalysts for PEMFC applications and at very least provided a tool to pre-condition the pristine $Pt_{ML}/Pd/C$ catalyst to form a complete Pt_{ML}.

Conclusions

In summary, by combining the electrochemical experiments with the physical characterizations and model analyses, we demonstrated the dynamic structural evolution of the $Pt_{ML}/Pd/C$ core-shell catalyst in the ORR that determined its mass-, specific-, and dollar-activities, ECSA, and reliability. Its ORR activity showed a volcano-like profile during the course of a 100k-cycle stability test; the mass/dollar activity eventually registered as high as 83% of the initial value. The activity increased until the end of the first 20k cycles because the freshly-prepared Pt monolayer arranged all the atoms only on the four-fold and three-fold hollow sites of the surface Pd, and, upon the ORR it shrunk into a full coverage on the Pd core that facilitated the dissociative adsorption of oxygen. This process adequately demonstrates the self-healing ability of Pt_{ML} electrocatalysts. On the other hand, the subsequent activity loss at a much lower rate than the standard Pt/C was due to the favorable Pd-Pt core-shell interaction and its structural self-retaining property that obviously retarded the electrochemical Ostwald ripening of the whole structure. Structural self-healing and self-retaining mechanisms accounted for the exceptionally high ORR stability of $Pt_{ML}/Pd/C$ electrocatalyst. The structure-dependent stability of the Pt_{ML}/Pd in the ORR pointed out a new avenue to designing ORR catalysts of pivotal importance for the development of most electrochemical energy frameworks.

Supplementary information

Model calculation details, additional electrochemical data, SEM-EDX, XPS and TEM analysis, and additional model-analyses data.

Conflicts of interest

There are no conflicts to declare.

Author Contributions

G. Chen, K. Sasaki, G. Yin and R. R. Adzic designed experiments; G. Chen, K. Sasaki, K. A. Kuttiyiel and D. Su carried out experiments and model calculation. G. Chen, M. Li, L. Du, C. Du, Y. Gao and W. Fei analyzed experimental results. G. Chen wrote the manuscript with support from K. Sasaki, K. A. Kuttiyiel and M. Li. All authors discussed the results and contributed to the final manuscript.

Acknowledgements

References

[1]   A. Iiyama, K. Shinohara, S. Iguchi and A. Daimaru, Membranes and catalyst performance targets for automotive fuel cells, in: W. Vielstich, A. Lamm, H.A. Gasteiger and H. Yokokawa (Eds.), *Handbook of Fuel Cells - Fundamentals, Technology, and Applications*, John Wiley & Sons, Chichester, 2010, vol. 6, pp. 905-915.

[2]   K. Sasaki, M. Shao and R. Adzic, Dissolution and stabilization of platinum in oxygen cathodes, in: F.N. Büchi, M. Inaba and T.J. Schmidt (Eds.), *Polymer Electrolyte Fuel Cell Durability*, Springer, New York, 2009, pp. 7-27.

[3]   M. K. Debe, *Nature*, 2012, **486**, 43-51.

[4]   J. Zhang, K. Sasaki, E. Sutter and R. R. Adzic, *Science*, 2007, **315**, 220-222.

[5]   R. Makharia, S. Kocha, P. Yu, M. A. Sweikart, W. Gu, F. Wagner and H. A. Gasteiger, *ECS Trans*., 2006, **1**, 3-18.

[6]   S. Chen, H. A. Gasteiger, K. Hayakawa, T. Tada and Y. Shao-Horn, *J. Electrochem. Soc*., 2010, **157**, A82-A97.

[7]   C. Wang, D. van der Vliet, K. L. More, N. J. Zaluzec, S. Peng, S. Sun, H. Daimon, G. Wang, J. Greeley, J. Pearson, A. P. Paulikas, G. Karapetrov, D. Strmcnik, N. M. Markovic and V. R. Stamenkovic, *Nano Lett*., 2011, **11**, 919-926.

[8]   Y. Kang, J. Snyder, M. Chi, D. Li, K. L. More, N. M. Markovic and V. R. Stamenkovic, *Nano Lett*., 2014, **14**, 6361-6367.

[9]   X. Huang, Z. Zhao, L. Cao, Y. Chen, E. Zhu, Z. Lin, M. Li, A. Yan, A. Zettl, Y. M. Wang, X. Duan, T. Mueller and Y. Huang, *Science*, 2015, **348**, 1230-1234.

[10] K. Sasaki, H. Naohara, Y. Cai, Y. M. Choi, P. Liu, M. B. Vukmirovic, J. X. Wang and R. R. Adzic, *Angew. Chem. Int. Ed*., 2010, **49**, 8602-8607.

[11] K. Sasaki, H. Naohara, Y. M. Choi, Y. Cai, W. F. Chen, P. Liu and R. R. Adzic, *Nat. Commun*., 2012, **3**, 1115.

[12] US DOE, Fuel Cell Technologies Program: Multi-Year Research, Development, and Demonstration Plan - Planned program activities for 2011-2020 <https://www.energy.gov/sites/prod/files/2017/05/f34/fcto_myrdd_fuel_cells.pdf>, 2017.

[13] Y. Shao-Horn, W. C. Sheng, S. Chen, P. J. Ferreira, E. F. Holby and D. Morgan, *Top. Catal*., 2007, **46**, 285-305.

[14] P. J. Ferreira, G. J. la O', Y. Shao-Horn, D. Morgan, R. Makharia, S. Kocha and H. A. Gasteiger, *J. Electrochem. Soc*., 2005, **152**, A2256-A2271.

[15] R. Borup, J. Meyers, B. Pivovar, Y. S. Kim, R. Mukundan, N. Garland, D. Myers, M. Wilson, F. Garzon, D. Wood, P. Zelenay, K. More, K. Stroh, T. Zawodzinski, J. Boncella, J. E. McGrath, M. Inaba, K. Miyatake, M. Hori, K. Ota, Z. Ogumi, S. Miyata, A. Nishikata, Z. Siroma, Y. Uchimoto, K. Yasuda, K. I. Kimijima and N. Iwashita, *Chem. Rev*., 2007, **107**, 3904-3951.

[16] S. R. Brankovic, J. X. Wang and R. R. Adžić, *Surf. Sci.*, 2001, **474**, L173-L179.

[17] K. A. Kuttiyiel, K. Sasaki, Y. Choi, D. Su, P. Liu and R. R. Adzic, *Energ. Environ. Sci.*, 2012, **5**, 5297-5304.

[18] K. Sasaki, J. X. Wang, H. Naohara, N. Marinkovic, K. More, H. Inada and R. R. Adzic, *Electrochim. Acta*, 2010, **55**, 2645-2652.

[19] NE Chemcat licenses Brookhaven catalyst tech for auto fuel cells, *Fuel Cells Bull.*, 2012, **2012**, 10-11.

[20] J. Zhang, M. B. Vukmirovic, Y. Xu, M. Mavrikakis and R. R. Adzic, *Angew. Chem. Int. Ed.*, 2005, **44**, 2132-2135.

[21] K. Sasaki, N. Marinkovic, H. S. Isaacs and R. R. Adzic, *ACS Catal.*, 2016, **6**, 69-76.

[22] T. J. Schmidt and H. A. Gasteiger, Rotating thin-film method for supported catalysts, in: W. Vielstich, A. Lamm and H. A. Gasteiger (Eds.), *Handbook of Fuel Cells - Fundamentals, Technology, and Applications*, John Wiley & Sons, Chichester, 2003, vol. 2, pp. 316-333.

[23] Y. Garsany, O. A. Baturina, K. E. Swider-Lyons and S. S. Kocha, *Anal. Chem.*, 2010, **82**, 6321-6328.

[24] H. A. Gasteiger, S. S. Kocha, B. Sompalli and F. T. Wagner, *Appl. Catal. B: Environ.*, 2005, **56**, 9-35.

[25] I. E. L. Stephens, A. S. Bondarenko, U. Grønbjerg, J. Rossmeisl and I. Chorkendorff, *Energ. Environ. Sci.*, 2012, **5**, 6744-6762.

[26] J. X. Wang, H. Inada, L. Wu, Y. Zhu, Y. Choi, P. Liu, W. Zhou and R. R. Adzic, *J. Am. Chem. Soc.*, 2009, **131**, 17298-17302.

[27] K. A. Kuttiyiel, K. Sasaki, D. Su, M. B. Vukmirovic, N. S. Marinkovic and R. R. Adzic, *Electrochim. Acta*, 2013, **110**, 267-272.

[28] D. van der Vliet, D. S. Strmcnik, C. Wang, V. R. Stamenkovic, N. M. Markovic and M. T. M. Koper, *J. Electroanal. Chem.*, 2010, **647**, 29-34.

[29] S. M. Alia, K. O. Jensen, B. S. Pivovar and Y. Yan, *ACS Catal.*, 2012, **2**, 858-863.

[30] Z. Zhang, K. L. More, K. Sun, Z. Wu and W. Li, *Chem. Mater.*, 2011, **23**, 1570-1577.

[31] M. Shao, A. Peles and K. Shoemaker, *Nano Lett.*, 2011, **11**, 3714-3719.

[32] F. J. Perez-Alonso, D. N. McCarthy, A. Nierhoff, P. Hernandez-Fernandez, C. Strebel, I. E. L. Stephens, J. H. Nielsen and I. Chorkendorff, *Angew. Chem. Int. Ed.*, 2012, **51**, 4641-4643.

[33] C. J. Powell and A. Jablonski, *NIST Electron Inelastic-Mean-Free-Path Database*, Version 1.2, National Institute of Standards and Technology, Gaithersburg, 2010.

[34] J. Okada, J. Inukai and K. Itaya, *Phys. Chem. Chem. Phys.*, 2001, **3**, 3297-3302.

[35] N. M. Marković and P. N. Ross, *Surf. Sci. Rep.*, 2002, **45**, 121-229.

[36] A. Cuesta, L. A. Kibler and D. M. Kolb, *J. Electroanal. Chem.*, 1999, **466**, 165-168.

[37] R. R. Adzic, *Electrocatal.*, 2012, **3**, 163-169.

[38] J. Erlebacher, M. J. Aziz, A. Karma, N. Dimitrov and K. Sieradzki, *Nature*, 2001, **410**, 450-453.

[39] D. Wang, Y. Yu, H. L. Xin, R. Hovden, P. Ercius, J. A. Mundy, H. Chen, J. H. Richard, D. A. Muller, F. J. DiSalvo and H. D. Abruña, *Nano Lett.*, 2012, **12**, 5230-5238.

[40] N. Aoki, H. Inoue, T. Okawa, Y. Ikehata, A. Shirai, H. Daimon, T. Doi, Y. Orikasa, Y. Uchimoto, H. Jinnai, S. Inamoto, Y. Otsuka and M. Inaba, *Electrocatal.*, 2018, **9**, 125-138.

[41] N. Todoroki, Y. Bando, Y. Tani, S. Kaneko, H. Watanabe, S. Takahashi and T. Wadayama, *J. Electrochem. Soc.*, 2017, **164**, F908-F910.

[42] J. Greeley, I. E. L. Stephens, A. S. Bondarenko, T. P. Johansson, H. A. Hansen, T. F. Jaramillo, J. Rossmeisl, I. Chorkendorff and J. K. Nørskov, *Nat. Chem.*, 2009, **1**, 552-556.

[43] A. V. Ruban, H. L. Skriver and J. K. Nørskov, *Phys. Rev. B*, 1999, **59**, 15990-16000.

[44] K. J. J. Mayrhofer, K. Hartl, V. Juhart and M. Arenz, *J. Am. Chem. Soc.*, 2009, **131**, 16348-16349.

[45] G. E. Ramírez-Caballero and P. B. Balbuena, *J. Phys. Chem. Lett.*, 2010, **1**, 724-728.

[46] M. K. Carpenter, T. E. Moylan, R. S. Kukreja, M. H. Atwan and M. M. Tessema, *J. Am. Chem. Soc.*, 2012, **134**, 8535-8542.

[47] K. D. Beard, D. Borrelli, A. M. Cramer, D. Blom, J. W. Van Zee and J. R. Monnier, *ACS Nano*, 2009, **3**, 2841-2853.

[48] J. K. Nørskov, J. Rossmeisl, A. Logadottir, L. Lindqvist, J. R. Kitchin, T. Bligaard and H. Jónsson, *J. Phys. Chem. B*, 2004, **108**, 17886-17892.

[49] G. E. Ramírez-Caballero, Y. Ma, R. Callejas-Tovar and P. B. Balbuena, *Phys. Chem. Chem. Phys.*, 2010, **12**, 2209-2218.

[50] P. B. Balbuena, R. Callejas-Tovar, P. Hirunsit, J. M. Martínez de la Hoz, Y. Ma and G. E. Ramírez-Caballero, *Top. Catal.*, 2012, **55**, 322-335.

[51] L. Gan, M. Heggen, R. O'Malley, B. Theobald and P. Strasser, *Nano Lett.*, 2013, **13**, 1131-1138.

[52] L. Dubau, F. Maillard, M. Chatenet, J. André and E. Rossinot, *Electrochim. Acta*, 2010, **56**, 776-783.

[53] D. A. Cantane, F. E. R. Oliveira, S. F. Santos and F. H. B. Lima, *Appl. Catal. B: Environ.*, 2013, **136**, 351-360.

[54] W. An and P. Liu, *J. Phys. Chem. C*, 2013, **117**, 16144-16149.

[55] L. Zhang, R. Iyyamperumal, D. F. Yancey, R. M. Crooks and G. Henkelman, *ACS Nano*, 2013, **7**, 9168-9172.

[56] S. E. Habas, H. Lee, V. Radmilovic, G. A. Somorjai and P. Yang, *Nat. Mater.*, 2007, **6**, 692-697.

Graphical abstract

The structure-activity relationship of Pd-Pt$_{ML}$ core-shell electrocatalyst for the oxygen reduction reaction during up to 100k cycles of stability test is elucidated, and a new mechanism, the self-healing and self-retaining mechanism, is proposed to illuminate the ultra-high ORR stability of Pt$_{ML}$ electrocatalysts.